

AUTOMATED DETECTION OF GALAXY-SCALE GRAVITATIONAL LENSES IN HIGH-RESOLUTION IMAGING DATA

PHILIP J. MARSHALL^{1,2}, DAVID W. HOGG³, LEONIDAS A. MOUSTAKAS⁴, CHRISTOPHER D. FASSNACHT⁵,
MARUŠA BRADAČ^{1,2,*}, TIM SCHRABBACK^{6,7}, AND ROGER D. BLANDFORD²

Draft version October 29, 2018

ABSTRACT

Direct lens modeling is the key to successful and meaningful automated strong galaxy-scale gravitational lens detection. We have implemented a lens-modeling “robot” that treats every bright red galaxy (BRG) in a large imaging survey as a potential gravitational lens system. Using a simple model optimized for “typical” galaxy-scale gravitational lenses, we maximize the multiply-imaged source plane flux and generate, for the resulting best lens model, four assessments of model quality that are then used in an automated classification. The robot infers from these four data the lens classification parameter H that a human would have assigned; the inference is performed using a probability distribution generated from a human-classified training set of candidates, including realistic simulated lenses and known false positives drawn from the *HST* Extended Groth Strip (EGS) survey. We compute the expected purity, completeness and rejection rate, and find that these statistics can be optimized for a particular application by changing the prior probability distribution for H ; this is equivalent to defining the robot’s “character.” Adopting a realistic prior based on expectations for the abundance of lenses, we find that a lens sample may be generated that is $\sim 100\%$ pure, but only $\sim 20\%$ complete. This shortfall is due primarily to the over-simplicity of the lens model. With a more optimistic robot, $\sim 90\%$ completeness can be achieved while rejecting $\sim 90\%$ of the candidate objects. The remaining candidates must be classified by human inspectors. Displaying the images used and produced by the robot on a custom “one-click” web interface, we are able to inspect and classify lens candidates at a rate of a few seconds per system, suggesting that a future 1000 square degree imaging survey containing 10^7 BRGs, and some 10^4 lenses, could be successfully, and reproducibly, searched in a modest amount of time. We have verified our projected survey statistics, albeit at low significance, using the *HST*/EGS data, discovering four new lens candidates in the process.

Subject headings: gravitational lensing – methods: data analysis – methods: statistical – techniques: miscellaneous – galaxies: elliptical – surveys

1. INTRODUCTION

Large, well-defined samples of strong gravitational lenses enable many important astrophysical and cosmological investigations. These include measuring the projected dark and luminous mass distributions of galaxies (e.g. Treu & Koopmans 2004; Koopmans et al. 2006), measuring the expansion rate of the universe $H(z)$ with lens time delays (e.g. Suyu et al. 2008; Oguri 2007), and also cosmological volumes and distance ratios (e.g. Mitchell et al. 2005; Capelo & Natarajan 2007), and probing the dark galaxy substructure predicted by CDM models (Kochanek & Dalal 2004; Bradač et al. 2004). Extended lensed source galaxy images provide more constraints on the lens mass distribution (e.g. Koopmans 2005) than do lensed point sources. Since lensing con-

serves surface brightness, the distant lensed (“source”) objects are greatly extended and magnified, revealing details that may not be otherwise visible. For example, recent observations using gravitational lenses as “cosmic telescopes” have provided unprecedented views of forming dwarf galaxies (e.g. Marshall et al. 2007), Lyman-break galaxies at $z = 2 - 4$ (see e.g. Bunker et al. 2000; Smail et al. 2007; Allam et al. 2007), and quasar accretion disks (e.g. Poindexter et al. 2008). Having a large array of cosmic telescopes will allow us to select the best ones for any given application, but will also allow us to build up a statistical picture of the source population.

Since the first strong lens was discovered, (Q 0957+561, Walsh et al. 1979), the ~ 200 galaxy-scale lenses known have been found by a combination of serendipitous discovery and a host of systematic search techniques. These techniques include visual inspection of deep optical imaging obtained with the *Hubble Space Telescope* (*HST*; e.g. Hogg et al. 1996; Zepf et al. 1997; Ratnatunga et al. 1999; Fassnacht et al. 2004; Moustakas et al. 2007; Faure et al. 2008), targeted imaging of the population of potentially lensed quasars or radio sources (e.g. Myers et al. 2003; Browne et al. 2003; Inada et al. 2003; Oguri et al. 2004; Pindor et al. 2006), and followup of systems for which optical spectroscopy revealed anomalous emission lines (e.g. Warren et al. 1996; Bolton et al. 2004; Willis et al. 2006). Further techniques using time-domain information have been

¹ Physics department, University of California, Santa Barbara, CA 93601, e-mail: pjm@physics.ucsb.edu

² KIPAC, P.O. Box 20450, MS29, Stanford, CA 94309

³ Center for Cosmology and Particle Physics, Department of Physics, New York University, 4 Washington Place, New York, NY 10003

⁴ JPL/Caltech, 4800 Oak Grove Dr, MS 169-327, Pasadena, CA 91109

⁵ Department of Physics, U.C. Davis, Davis, CA 95616

⁶ Argelander-Institut für Astronomie, Universität Bonn, Auf dem Hügel 71, 53121 Bonn, Germany

⁷ Leiden Observatory, Leiden University, Niels Bohrweg 2, 2333 CA Leiden, The Netherlands

* Hubble Fellow

proposed as efficient lens finders (e.g. Pindor 2005; Kochanek et al. 2006).

It is a spectroscopic survey that has generated the largest single lens sample to date. With the SDSS galaxy redshift survey as its feeder, the Sloan-Lens ACS Survey (SLACS) project (Bolton et al. 2006) has discovered ~ 70 new galaxy-scale strong lenses (Bolton et al. 2008). Candidates are selected for their background galaxy emission lines present in the foreground old stellar population spectrum, and then confirmed using high resolution *HST* imaging. The SDSS selection function limits the median lens redshift to be ≈ 0.2 , while the need for detectable emission lines hides many lenses and incurs a strong “magnification bias” towards ring-like systems. Future surveys will extend the lens redshift limit somewhat, but likely not reach the same area as SDSS.

Instead, we anticipate that samples of galaxy-scale gravitational lenses that are 2-3 orders of magnitude larger than the current set will come, at least before SKA, from large optical imaging surveys. For example, the proposed Super-Nova Acceleration Probe (SNAP) mission is slated to include a 1000 square degree survey at *HST*/WFPC2 resolution (Aldering et al. 2004; Marshall et al. 2005a), with multi-band imaging to provide photometric redshifts of faint galaxies, and discover some 10^4 strong lenses. From the ground, KIDS, Pan-STARRS, DES and LSST will all make significant advances in strong lensing, but will be limited by their angular resolution: their strengths will lie in the finding of large numbers of time-varying, and/or wide-separation, lensed systems. The majority of the strong lensing cross-section in the universe lies in massive elliptical galaxies (Turner et al. 1984). Therefore, in a high-resolution space-based survey, the majority of lenses will be massive elliptical galaxies with redshifts 0.5–1.0, multiply-imaging faint blue star-forming galaxies at redshifts 1.0 and above (e.g. Marshall et al. 2005a). This suggests that an efficient strategy is to focus on bright red galaxies (BRGs) as being the “typical” potential lenses (e.g. Fassnacht et al. 2004; Faure et al. 2008).

Cost limitations mean we may not be able to perform spectroscopy on all future lens candidates, whose sources are likely to be quite faint, and we will need to rely on a better, more quantitative understanding of the imaging data in hand. Indeed, with only image information available, the classification of any lens candidate must come entirely from modeling. Does a model for the image where some of the features are lensed by a massive object (consistent with the observed elliptical galaxy) explain the data? Are the residuals from this modeling process consistent with what we know about early-type galaxy structure? We suggest that the optimal way to *find* lenses in optical imaging surveys is to classify objects by their ability to be modeled as gravitational lenses.

In the imaging survey gravitational lens searches already carried out, the lens modeling has been performed *after* a sample of candidates has been generated by other means, and classified by experienced human inspectors. Indeed, this human inspection stage can be sufficiently effective that it can be thought of as an approximate lens-modeling process. Present-day *HST* surveys of area ~ 1 square degree are small enough that human inspection is tedious but feasible. However, looking forward to the next generation of high resolution imaging

surveys, and desiring to *build on* the extensive human expertise in identifying lenses, we are motivated to develop an automated lens-finding “software robot.” The tirelessness of this robot would enable it to find lenses with a well-understood, calculable, and reproducible selection function; this will be a vital property for the resulting lens samples to be statistically useful.

In this work, we describe just such a robot: it models every possible candidate massive galaxy image in the survey as a combination of foreground (lensing) galaxy and multiply-imaged background (lensed) source, and then interprets the results based on its previous experience with both real and simulated data. We will argue that, at least at present, the most effective automated methods mimic the operation of a human analyst: our robot attempts to predict, via a probabilistic model, the classification that would have been made by a human.

We can prepare for a future of much larger surveys by working with manageably-sized current samples of lens candidates from extant high resolution imaging surveys. The *HST* archive contains several square degrees of suitably-surveyed (e.g. deep, high galactic latitude) sky, which we are searching for serendipitous lensing events (the HAGGLEs project, program HST-AR-10678 Marshall et al. 2005b, Marshall et al. in preparation). As a pilot for this project, we carried out a by-eye search for lenses in the 0.17 square degree area of the *HST*/ACS coverage of the Extended Groth Strip (EGS, Davis et al. 2007), finding three definite lenses (Moustakas et al. 2007, hereafter M07), which includes one that was found (also by eye) in the *HST* Medium Deep Survey (Ratnatunga et al. 1999), and four candidates of lower believability (Moustakas et al. 2006, hereafter M06). This dataset therefore makes an excellent testing ground for new lens detection methods.

This paper is organized as follows. In Sections 2 (lens modeling) and 3 (probabilistic interpretation) we outline our lens-finding algorithm, and describe its implementation as a software robot. In Section 4 we educate the robot, using a large set of simulated galaxy-scale lenses, and a roughly equal number of human-classified non-lenses from the *HST* EGS survey. As a step towards understanding the selection function of galaxy-galaxy strong lenses, we assess the completeness and purity of the robot-generated sample at this point. Then in Section 5, as a “blind test” we apply our automatic lens finder to the remaining EGS images used in M06 and M07, and compare with the by-eye search results. Following some discussion of the strengths and weaknesses of our approach in Section 6, we present our conclusions in Section 7. All magnitudes referred to are calculated in the AB system.

2. LENS MODELING

From a given potential lens galaxy, suitably selected (e.g. by color and magnitude) and extracted from the survey images, we subtract a smooth, symmetric model of its own intensity, leaving a residual map that may potentially (and perhaps partially) be explained by multiple images of a background source. For each possible lens model in a finite, gridded space, we compute gravitational lens deflections that are used to transform the observed (“image-plane”) pixels to their nearest-pixel unlensed (“source-plane”) positions. Because the models

under consideration are multiply-imaging, more than one image-plane pixel may map to each source-plane pixel; since gravitational lensing conserves surface brightness, the pixels of the image plane mapping to the same point in the source plane should have equal values. To optimize the model we construct a scalar that is maximized when non-trivial fractions of image-plane pixels “agree” on the intensity to be assigned to these source-plane pixels. The bright and dark parts of the residual maps both participate in this agreement; indeed, blank sky in the image plane where a second, third, or fourth image ought to appear, given structure in the source plane, is more damning to a possible lens model than image-plane flux where no image is expected, and our scalar metric captures this.

The method is motivated by the observation that when multiply-imaged galaxies are faint, the best evidence that they are indeed multiply-imaged is that there is a reasonable gravitational lens model with a reasonable unlensed intensity pattern that describes the morphology as observed.

In order to make best use of the reader’s attention span we give a very brief overview of our lens modeling procedure below, and then expand on the technical details in subsection 2.2. We expect many might discreetly push ahead to Section 3 at this point.

2.1. Overview of modeling procedure

- We assume that most strong lensing galaxies have the smooth, symmetric morphologies of early-type galaxies, and subtract off the best-fitting set of concentric elliptical isophotes. In practice we fit an elliptically-symmetric Moffat profile, which is very effective at removing galaxy bulges. Many bright red galaxies do show some disk component in their images; we identify these by their position and orientation relative to the major axis of the bulge, and mask out all pixels associated with the features.
- We assume that these galaxies’ lens potentials can be modeled adequately with singular isothermal sphere models plus external shear, and we grid this 3-dimensional parameter space with a coarse pixelization. The motivation for using this simple model is partly empirical, based on the results from the SLACS project (Koopmans et al. 2006), and partly to keep the CPU time manageable.
- We assume that the background source sizes, or angular scale over which background sources vary, is comparable to, or larger than the *HST* point spread function (PSF), and consequently ignore the latter when tracing flux back to the source plane. With any given lens model we perform a very crude ray-tracing to map image plane pixels onto a (finer) grid of source pixels.
- In any putative multiple-imaging system, we require (for identification as a lens) that at least some of the detected residuals lying in the multiply-imaged part of the image plane be explained by a multiply-imaged background source.
- When mapping a set of multiply-imaged image-plane pixels back to the same source plane pixel,

we take the minimum value of the image pixels’ fluxes. This allows us to use all the information in the image, using dark sky to veto non-lensed bright sky.

- Stepping through the entire grid of models, we select the one that maximizes this “minimum-filtered” source plane flux as our “optimal” model.

2.2. Technical notes

The image-plane and source-plane pixel grids we choose are determined by the pixelization of the input image. We use drizzled *HST*/ACS images with pixel scale 0.03 arcsec, and investigate 6 arcsec cutout images centered on a pre-selected elliptical galaxy position. This selection is an important part of the lens search: one may consider using both color and morphology to pre-select elliptical galaxies, although this process is made considerably harder by the (possible) presence of the contrasting lensed images themselves. In this work we adopt the inclusive approach of investigating all bright extended objects, and exploring the performance of our technique on the selection criteria involved. To reduce computation time, and improve the accuracy of the ray-tracing, we bin the image plane by a factor of two. This reduces the number of deflection angles to be calculated by a factor of four (and further justifies our ignoring the PSF at this stage).

The grid of model space we choose for the lensing potential is three-dimensional: we use a singular isothermal sphere (SIS) with external shear (e.g. Kochanek 1991; Kormann et al. 1994). The primary parameter is the SIS lens strength, specified as the angular Einstein radius θ_E . Having a more subtle effect on the lensing behavior are the two parameters that describe the magnitude and direction of the external shear, γ_X and ϕ_X . These two parameters are vital, since a significant fraction of all known lenses are four image systems (quads). Without the external shear the SIS model can only produce two images. All points in this parameter space are treated as being equally likely prior to fitting each source, and are then stepped through in an exhaustive search. The coarseness of the grid was chosen to keep the CPU time per system low. We restricted the Einstein radius to lie between 0.4 and 1.8 arcsec, large enough to include all SIS lenses with velocity dispersion in the range 160 to 350 km/s (given a lens at $z_d = 0.5$ and a source at redshift $z_s = 1.0$).

For each lens model we trace the image plane pixel values back to the source plane via the usual lens equation,

$$\boldsymbol{\beta} = \boldsymbol{\theta} - \boldsymbol{\alpha} \quad (1)$$

where the optical axis was taken to be the centroid of the elliptical galaxy light, and the two components of the deflection angle $\boldsymbol{\alpha}$ are given by

$$\alpha_1 = \theta_1 \frac{\theta_E}{|\boldsymbol{\theta}|} + \gamma_X (\theta_1 \cos 2\phi_X + \theta_2 \sin 2\phi_X) \quad (2)$$

$$\alpha_2 = \theta_2 \frac{\theta_E}{|\boldsymbol{\theta}|} + \gamma_X (\theta_1 \sin 2\phi_X - \theta_2 \cos 2\phi_X) \quad (3)$$

We use nearest-neighbor mappings; that is, we “snap” the lensing deflections “to grid.” This is a time-saving device: rather than having square pixels in the image

plane map to distorted rectangles in the source plane, we are crudely approximating the source using a square grid. We will discuss the effects of this approximation in Section 4.5; here we note that we do at least use a source plane that is twice as finely gridded as the (binned) image plane.

We are specifically interested in multiple-image systems: some source-plane pixels will have more than one associated image-plane pixel mapping to each one, and in general those associated image-plane pixels will come from widely separated locations on the image plane. For each pixel in the source plane, we record the *minimum* intensity of the contributing image-plane pixels. In this “minimum-filtered” map, any image-plane pixel that is blank or low in intensity effectively “vetoes” any other contributions to the source-plane intensity in that pixel. For this reason, the minimum map in fact represents (in the absence of noise and pixelization effects) the only source-plane flux that can be contributing to the residual map, consistent with the multiply imaging lens potential model under consideration. This simple estimator compensates for our inability to model simultaneously and effectively all the features in the image, and focuses directly on the component of the image we are interested in: the gravitationally-lensed component.

When locating the best lens model for a given system, the scalar objective function we compute is simply the total flux in the minimum-filtered source plane. In many cases we expect this scalar to be zero, as the minimum filtering removes all unlensed flux: this is certainly true of the blank parts of the image that are truly blank (rather than containing sky noise). For this reason we “de-noise” the galaxy-subtracted images by setting all pixels not containing significant flux to zero. This thresholding is done with standard object detection software (SExtractor, Bertin & Arnouts 1996), which associates pixels together into objects and flags the remainder as background. Specifically, we use the “objects” checkimage output as our data.

At each value of the model Einstein radii θ_E , we maximize the source plane flux by stepping through the external shear parameters. This allows us to plot source plane flux versus θ_E . The optimal model is then the one corresponding to the peak of this plot.

2.3. Multi-filter data

So far we have made no mention of the achromatic nature of gravitational lensing, yet this is one of the most important pieces of information at the disposal of any by-eye lens searcher. This is because the human eye is very good at detecting subtle changes in color, and in picking out objects of a given color from a noisy background. However, the achromaticity is a direct result of surface brightness being conserved at all wavelengths; up until this point we have just described using surface brightness conservation in one band. If imaging data in more than one band is available to us, how should we include this information? We expect the source morphology to be different between the different bands, so the lens inversions should be done independently. However, it must be the same mass distribution giving rise to any lensing effects detected.

The correct thing to do when analyzing the independent datasets (in this case, the images in different filters)

is to add the log likelihoods for each band’s image together. Dropouts (sources with no detected flux in one of the bands) will rightly contribute zero to the summed log likelihood. For computational efficiency we are not optimizing the lens model by maximizing its likelihood, but we can compute the likelihood of the “optimal” model once it has been obtained. In Section 3 below we will do exactly this – and combine the likelihoods from the different filters images as well. While multiple bands can be analyzed in this straightforward way, we note that our method does not rely on having multi-filter data – although we expect performance to improve in the multi-filter case.

One use of any additional filters could be in improving the pre-selection of candidate elliptical galaxies. Another is that the redder images tend to give more accurate lens galaxy centroids (since the redder images have more regular morphologies better tracing the dark matter halo).

2.4. Modeling examples

In Figure 1 we show three example bright red galaxies (drawn from the EGS survey, see Section 5), and their automated analysis. One is a lens (visually selected by M07), and two are potential false positives showing confusing “lens plane” structure. In each case the robot is able to find a lens model that explains *some* of the observed galaxy-subtracted residuals, but with varying goodness of fit; in the next section we describe how we use this and other information from the robot to make an automated classification.

3. AUTOMATED LENS CANDIDATE CLASSIFICATION

Given an optimized lens model, we now generate a set of data describing the quality of the model in describing the observed image. A classification parameter can then be inferred from this robot output data vector \mathbf{d} , whose components we describe below.

3.1. The robot’s output: quantifying lens model quality

The source plane flux scalar described above is simple, and fast, to calculate. However, a much better-understood objective function is the log likelihood of the predicted source model. To calculate this, we invert the lens mapping to produce the corresponding image counts predicted by the lens and source model, I^P . Assuming the Gaussian approximation to the Poisson distribution for the (assumed uncorrelated) pixel noise on the data image counts I , the log likelihood is given by

$$-2 \log L = \sum_i \frac{(I_i - bI_i^P)^2}{\sigma_i^2}. \quad (4)$$

The uncertainty σ_i is estimated by adding in quadrature the root mean square pixel value measured in the background regions, to the square root of the i^{th} detected pixel value (thus taking into account, at least approximately, the Poisson noise due to the objects themselves). We add a further term, also in quadrature, to attempt to model the errors incurred by our very simple lens and coarsely-gridded source models: since the inadequacies of our model are independent of the quality of the data, we assume the modeling error will impose a signal-to-noise ratio floor a , so that its contribution to the overall uncertainty can be (crudely) approximated by I_i/a . We find

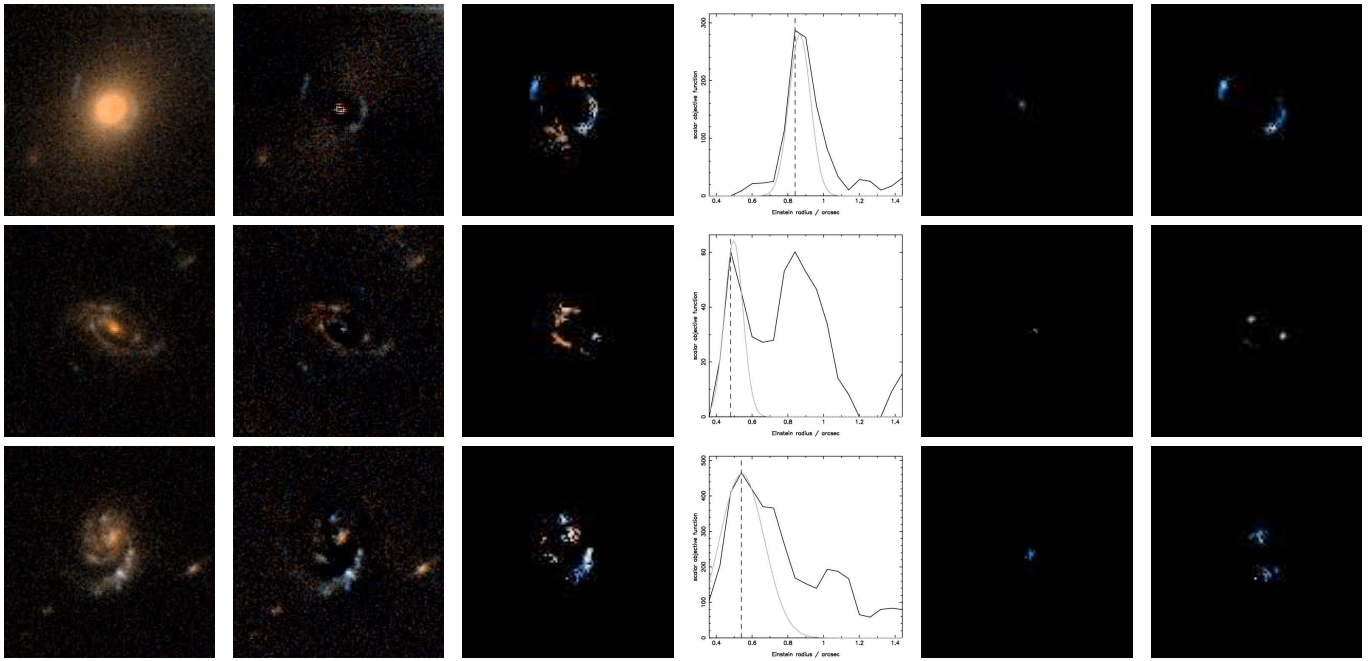


FIG. 1.— Robot modeling inputs and outputs for three example objects from the EGS survey, one in each row of panels: Top row, the “Anchor” gravitational lens found by eye by Moustakas et al. (2007); middle and bottom rows, potential false positives, showing confusing lens plane spiral arm structures, some of whose flux is consistent with having been lensed. In each row, numbering the panels from the left, we have: 1) the raw *HST* color cutout image; 2) the image after subtraction of a Moffat-profile model for the lens galaxy light; 3) the thresholded image input to the lens modeling robot; 4) the scalar objective function (minimum-filtered source plane flux, see text) plotted as function of Einstein radius and optimized over the external shear parameters; 5) the optimal model source plane; 6) the corresponding image plane. The images in panels 3 and 6 are used in computing the goodness of fit statistic n_σ (Section 3.1). Likewise, in panel 4 a Gaussian has been fitted to the peak of the scalar for the purposes of estimating the uncertainty on the Einstein radius, $\delta\theta_E$, and the detection ratio R_d . All cutout images are 6 arcsec on a side.

that $a = 4$ gives reasonable values of $\log L$ for a range of data quality. In summary,

$$\sigma_i^2 = \text{rms}^2 + I_i + (I_i/a)^2. \quad (5)$$

The sum in equation 4 is over all non-zero pixels in the predicted image, since we are only attempting to explain the flux in the multiply-imaged region around the putative lens. In principle, one could use the presence of additional residual image structure that was not compatible with being lensed as evidence that perhaps there is no lensing occurring at all. However, we prefer at this stage to be inclusive in the generated candidate list and only consider pixels in the multiple-imaging regime. The parameter b is a rescaling factor that allows us to correct the bias towards low source flux introduced by the use of the minimum-filtered source plane intensity when computing the predicted image I^P . We approximately marginalize this parameter out by using the value of b that maximizes $\log L$.

The left-hand side of equation 4 is distributed as chi-squared for approximately N degrees of freedom, where N is the number of non-zero pixels in the predicted image minus three model parameters. Therefore, we record the goodness of fit as the number of standard deviations n_σ this scalar is from the mean of the chi-squared distribution, using the Fisher approximation for large N : $\Pr(2\chi^2|N) \approx G(2N - 1, 1)$ (where $G(m, w)$ is a Gaussian distribution of mean m and standard deviation w). The image-plane likelihood evaluation is time consuming; however, as we use the source plane flux scalar to quickly determine the “best” model, we need only compute n_σ once. The n_σ is the first component of the robot output data vector \mathbf{d} .

Our coarse parameter grid and simple lens model become increasingly ill-suited to the data as the source size decreases. For us to detect any flux in the source plane the mass model must be good enough to map the pixels back to the same point with sub-pixel precision. We are helped by the PSF here, which spreads the flux around in the image plane, but the resulting minimum source plane produces a very sparse image plane. We account for this in the likelihood evaluation by applying a “restoring beam” to the predicted image. This beam is a Gaussian with FWHM slightly less than that of the ACS PSF, and produces more realistic image configurations. Since we originally mapped the *convolved* flux back to the source plane, we do the restoring convolution such that the peak surface brightness of the source plane is preserved into the predicted, convolved, image plane.

The parameter n_σ is clearly a powerful tool for quantifying how good a fit to the data a lens model provides. However, it does not tell the whole story. For example, very faint sources give very faint fluctuations in the image plane, which can often easily be fitted within the noise by a lens model. However, a human classifier is unlikely to assign this candidate a high score. We therefore make the magnitude of the source the second component of \mathbf{d} . We also add two more quantities. First is the uncertainty on the lens model Einstein radius, $\delta\theta_E$: a convincing lens model should give a very small $\delta\theta_E$. We estimate this from a Gaussian approximation to the peak in the plot of source plane flux against Einstein radius (Figure 1, panel 4). The second is related to this but subtly different: in a clean lens with just one source plane, we expect only one lens model to match the data, and so this same plot should have only one sharp peak. Therefore, as our

final \mathbf{d} -component we take the ratio R_d of the integral under the Gaussian fit to the integral under the whole source flux curve.

The four scalars described here that comprise \mathbf{d} were chosen purely for their intuitive information content. We are not suggesting they form a complete set, or that they have been optimized for this application – only that they are likely to provide some discriminatory power between different candidates. Indeed, we anticipate that much of the future work improving the performance of the robot might center on generating better \mathbf{d} -vectors, and so improving the “capacity” of the robot to *learn*. We will return to this issue in Section 6.

We list the robot outputs \mathbf{d} for the three examples shown in Figure 1 in Table 1 – this table illustrates some of the behavior suggested in the above discussion.

3.2. Inferring the human classification parameter

Having defined our set of scalars describing the quality of a lens model (the robot output \mathbf{d}), we must now decide on our criteria for assessing the robustness of each strong lens candidate. Before we continue, let us try to understand this last statement. Naively we might hope to quantify the quality of a lens candidate by seeking the “probability that it is a gravitational lens.” However, to calculate this it would also be necessary to compute the probability that the candidate is NOT a gravitational lens as well. The problem is that we do not yet have a sufficiently detailed and quantitative understanding of galaxy morphology to be able to do this. In the presence of disk components, spiral arms, satellite galaxies and so on, it is genuinely difficult to disentangle the contributions to the image from the lensed sources versus from the contribution from the candidate galaxy itself. Clearly, if the value of the detected source plane flux is zero then the system can be rejected. But we can expect a further continuum of likelihood values: if the robot is to succeed in returning a useful, shortened candidate list for our inspection, it must first learn what makes a good candidate.

While our quantification of galaxy structure is poor, our ability to identify gravitational lenses in high resolution images by eye is not. This suggests that a much better-defined measure of lens candidate robustness is the posterior probability distribution $\Pr(H|\mathbf{d})$, where H is the *classification that a human would have assigned the system*.

In Table 2 we propose a simple four-point system for human classification of gravitational lenses. Our experience is that fewer than four classes is not flexible enough to describe a set of lens candidates, while the differences between any more than four classes become too small for different classifiers to agree upon.

If we have a set of lens candidates, each with robot data vector \mathbf{d}_i and *known human class* H_i , then we can estimate the probability density function (PDF) $\Pr(\mathbf{d}|H)$ from these clouds of points in \mathbf{d} -space, H -value by H -value. We can then use this model PDF to compute $\Pr(\mathbf{d}_j|H)$ for the j^{th} candidate. $\Pr(H|\mathbf{d}_j)$ is given by Bayes’ Theorem,

$$\Pr(H|\mathbf{d}_j) \propto \Pr(\mathbf{d}_j|H)\Pr(H). \quad (6)$$

The prior PDF $\Pr(H)$ encodes our expectations for the relative frequencies of each human classification H . One

can imagine that there might be a great many low- H (poor quality) candidates and only a few high- H (and so very robust) candidates. In Section 4.4 below we will explore two quantified prior PDFs.

To make progress we now need to determine $\Pr(\mathbf{d}|H)$. For this we require a large sample of candidates, containing both lenses and non-lenses, and showing similar problems to real candidates. In the following subsection we describe the two sources of this *training set*, and the resulting education of our robot.

4. TRAINING THE ROBOT

Having implemented an efficient lens modeling robot, we now have to transfer to it our knowledge of lens, and more importantly, intrinsic BRG structure. The procedure is to generate a well-defined set of lens candidates whose human classification H is known, and that sample well the possible range of H -values.

4.1. Non-lenses in the EGS survey

The 63 ACS images⁹ of the 0.18 deg² *HST* mosaic of the Extended Groth Strip survey (EGS, Davis et al. 2007) were taken in both the F814W (“ I_{814} -band”) and F606W (“ V_{606} -band”) filters, to depths of 28.14 and 27.52 mag respectively (5- σ limits for point sources in 0.12 arcsec-radius circular measurement apertures). This survey contains a control sample of three strong lenses confirmed by their image modeling (and in two cases by spectroscopy as well), and four plausible strong lens candidates, all identified by an independent search by visual inspection of the ACS frames (M06 & M07). We will use this sample in Section 5 for comparison with our automated search results. Here, we aim to produce a catalog of BRGs that includes these known lenses, and then define a sample of known *non-lenses* with which to educate the robot.

To avoid any morphological bias in the candidate lens galaxies, we only minimally pre-filter the catalog of objects detected in the EGS fields, applying only a signal-to-noise and a color cut. Objects with $I_{814} \leq 22.0$ and $(V_{606} - I_{814}) > 0.8$ were selected, giving a sample of 1085 BRGs. All of the confirmed lenses, and three of the four lower-quality lens candidates, identified by M06 & M07 passed this cut. For our training set of non-lenses, we divided the 63 EGS fields into two sets, a training set of 3 fields, and a survey set of 60 fields. The three training fields were chosen to contain none of the lens M06/M07 candidates: the fields chosen were `egs2101`, `egs2102`, and `egs2103`. We then analyzed the 97 BRGs in these three training fields that passed our color-magnitude cut, generating optimized lens models for each object. These systems were classified by one of us (PJM), and binned by H -value.

4.2. Simulated lenses

Sampling BRGs that are lenses is harder – strong gravitational lenses are rare objects. Many of the known galaxy-scale lenses were found either via source-oriented radio source or quasar surveys (e.g. Browne et al. 2003; Oguri et al. 2006), or in unresolved spectroscopic surveys (e.g. Bolton et al. 2006); they tend to have either

⁹ Available from <http://aegis.ucolick.org>

TABLE 1
ROBOT OUTPUTS FOR THE THREE EXAMPLE LENS CANDIDATES IN FIGURE 1.

Object name	Position in Figure 1	n_σ	θ_E (arcsec)	$\delta\theta_E$ (arcsec)	R_d	Source magnitude AB, F606W	Human class (H)	Robot class (H_r)
HSTJ141833.11+524352.5	top	4.11	0.84	0.06	0.62	28.40	3	2.9
HSTJ141856.16+523843.5	middle	8.93	0.48	0.05	0.27	30.23	0	2.1
HSTJ141828.06+523646.1	bottom	21.56	0.54	0.12	0.56	27.96	0	1.4

TABLE 2
HUMAN LENS CLASSIFICATION SYSTEM USED IN THIS WORK.

Class H	Meaning
0	Definitely not a lens
1	Possibly a lens
2	Probably a lens
3	Definitely a lens

point-like or highly-magnified images, and are therefore not representative of the lenses we expect to find in high resolution imaging surveys.

The best training set for our purposes is then a sample of lenses whose properties match those of the lenses we expect to find in a high resolution optical imaging survey. To this end we simulated a realistic population of lenses and generated mock images of them. For the lenses, we used a set of 68 morphologically-selected early-type galaxies from the EGS survey ACS images. We made a very rough estimate of their redshift, by assuming a velocity dispersion of 220 km/s and using the Faber-Jackson relation to estimate luminosity, and so distance modulus given apparent I_{814} -band magnitude. We then drew a velocity dispersion from a Gaussian distribution of mean 220 km/s and width 20 km/s. The variety of redshifts and velocity dispersions is sufficient to give a reasonable distribution of Einstein radii. We also measured the position, ellipticity and orientation of the early-type galaxy light: these parameters were then used, along with the model velocity dispersion, to define an SIE model lens for each lens galaxy. To complete the lens model we added external shear with amplitude drawn from a log-normal distribution of mean 0.05 and width 0.6 (Holder & Schechter 2003), and external convergence equal to half the external shear magnitude.

For the sources, we drew faint galaxies from the EGS catalog, extracting their magnitudes, sizes, ellipticities and orientations and used these data to define a simple de Vaucouleurs (1948) bulge plus exponential disk model. We made a robust faint galaxy selection ($22 < I_{814} < 27$, and $0.15 \text{ arcsec} < \text{FWHM} < 0.36 \text{ arcsec}$) and approximately corrected the sizes for the ACS PSF by subtracting its Gaussian-approximated width in quadrature; the resulting corrected half-light radius was then asserted for both components of the disk+bulge model. We drew the disk/bulge ratio from a Gaussian of mean 3.0 and width 0.5, since we expect most faint blue source galaxies to be disk-like. For the source redshift we again approximated it using the I_{814} magnitude, following a simplified version of the recipe used by Massey et al. (2004b): $\text{Pr}(z_s)$ was assumed to be a Gaussian of width 0.4, centered on $z_m = 0.7 + 0.15(I_{814} - 22)$.

We generated a number of possible sources for each lens galaxy, providing more lens systems than early-type galaxies. Once we had both source and lens redshift, and SIE velocity dispersion parameter, we computed the

Einstein radii and rejected systems with $\theta_E < 0.4 \text{ arcsec}$ as being unobservable (Section 2.2). We then generated a source position drawn uniformly from a box of width $0.3\theta_E$ centered on a point offset by $(0.15, 0.15)\theta_E$ from the optical axis of the lens. This rather complex recipe was designed to avoid an overabundance of ring-like lenses while keeping us within the reasonably high magnification regime. Finally, we shuffled the list of simulated lens systems and selected the first 100 systems to make simulated images.

Figure 2 shows the redshift and magnitude distributions of the simulated lenses. The source redshifts can be seen to be roughly consistent with having been drawn from a distribution like that derived by Leauthaud et al. (2007) for the appropriate EGS magnitude limit, once the lensing (which favors higher source redshifts) has been taken into account. The magnitudes of the lenses are consistent with the bright (and hence massive) end of the early type population (as characterized using the morphologically-selected and spectroscopically-observed GOODS sample of Treu et al. 2005). The (unlensed) magnitudes of the sources are consistent with their parent EGS population, with the piling-up at magnitude 26 being due to a combination of the magnitude limit and the lensing shift to higher mean redshift.

We made mock, noise-free ACS images of the lensed images given the lens model described above; the process is the same as described (albeit in an inferential setting) in M07 and Marshall et al. (2007). We approximated the ACS PSFs by a Gaussian of $\text{FWHM} = 0.14 \text{ arcsec}$ and convolved the simulated images with this kernel, before adding it to the relevant EGS early-type galaxy image (in each filter). The resulting composite image has approximately the correct noise properties: we neglected the small contribution to the noise from the lensed images, as the lens galaxy surface brightness is often higher anyway. The end result is a set of 100 simulated lens galaxy cutout images that can be analyzed in an identical manner to the EGS lens candidates themselves. A gallery of examples is given in Figure 3.

4.3. Modeling $\text{Pr}(\mathbf{d}|H)$

We divided our training set (100 simulated lenses, plus 97 non-lenses from EGS) into 4 H -value bins, and for each H bin, plotted all of the robot output parameters in the vector \mathbf{d} against each other. These parameters were assumed to have been drawn from the distribution $\text{Pr}(\mathbf{d}|H)$; from the plots we estimated the number of modes of this PDF, and selected the samples associated with each mode by a series of orthogonal cuts in the values of \mathbf{d} . The modes were then modeled as multivariate Gaussians, defined by the means and covariance matrix of each mode. After normalizing each mode by the number of samples used to compute the properties of the mode, the overall PDF $\text{Pr}(\mathbf{d}|H)$ for that value of H is given by the simple sum of these Gaussian modes.

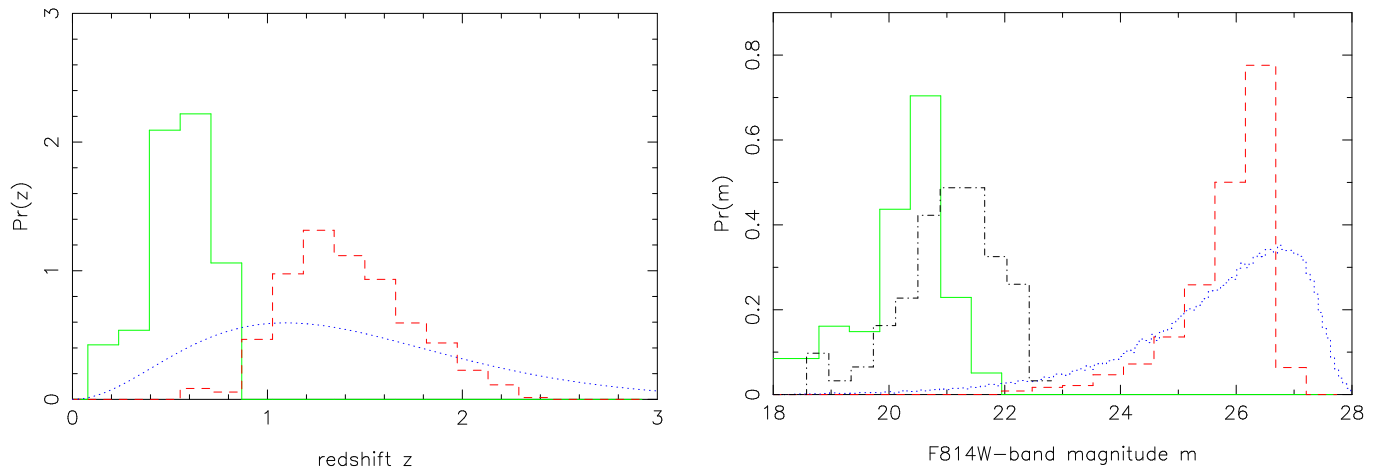


FIG. 2.— Redshift (left) and I_{814} -band magnitude (right) distributions for lens and source galaxies in the 100 simulated lens systems used in this paper. Green solid histograms show simulated lens galaxies, red dashed histograms show simulated source galaxies. Blue dotted curves show the parent source population – the redshift distribution from Leauthaud et al. (2007) and the EGS source counts. The black dot-dashed histogram is the morphologically-selected spheroidal sample from Treu et al. (2005).

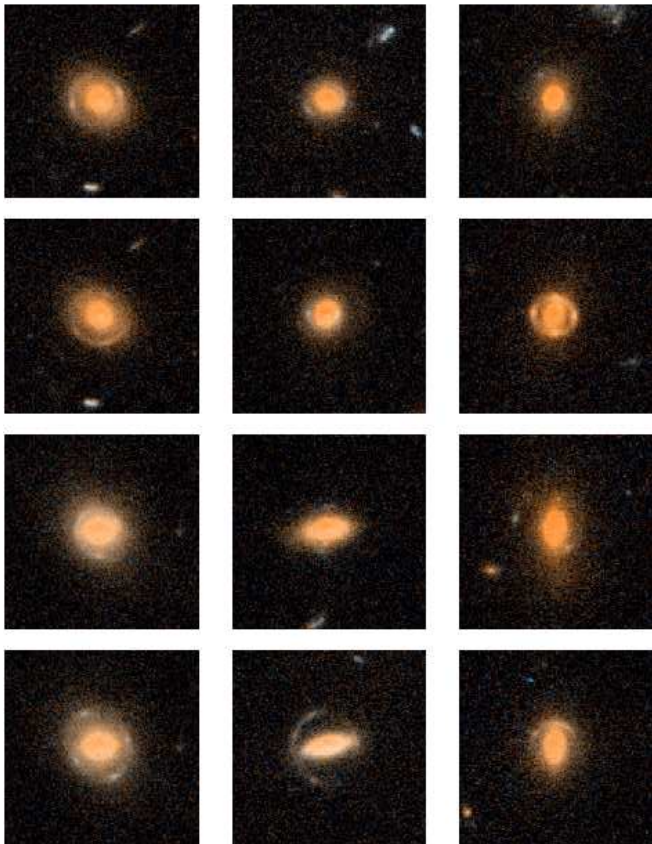


FIG. 3.— Mock EGS data for 12 example simulated gravitational lenses. All cutout images are 6 arcsec on a side.

In some cases the modes were broadened to provide a more satisfactory picture of the PDF; in some cases the Gaussian approximation breaks down leaving an ill-fitting distribution. This is of course a very subjective way of modeling the PDF, but this does not matter: all we are attempting to do is transfer our expertise to the robot such that it agrees with us in the generation of H -values. Since these are themselves subjective there seems little point in insisting on objectivity at every turn. While we can see there is room for improvement in the accuracy of the PDF model, the robot’s more important

quality is that of reproducibility: having taught it about human classification, the robot will be consistent in its own classification (unlike humans), such that a selection function can be estimated from realistic simulated data.

In Figures 4–7 we show plots of all four PDFs modeled in this way: $\Pr(\mathbf{d}|H = 0)$, $\Pr(\mathbf{d}|H = 1)$, $\Pr(\mathbf{d}|H = 2)$, and $\Pr(\mathbf{d}|H = 3)$. These plots provide the quantification of the common sense we would like the robot to have when inspecting lens candidates. In each panel, the contours enclose 68% and 95% of the marginalized probability density.

4.4. Robotic lens classification

In this Section we describe the automated classification of the training set, and estimate the completeness and purity of the resulting sample.

We use the PDFs described in the previous Section to compute the posterior PDF for the classification parameter H as follows:

$$\Pr(H|\mathbf{d}) \propto \sum_i \Pr(\mathbf{d}|H = i)\Pr(H = i), \quad (7)$$

and then choose as our estimator for H the posterior mean, denoted H_r (where “r” is for “robot”):

$$H_r = \frac{\sum_i i \Pr(H = i|\mathbf{d})}{\sum_i \Pr(H = i|\mathbf{d})}. \quad (8)$$

We note that H_r , the robot’s estimate of H , is a continuous variable even though H is not. In Section 5 below we combine human classification parameters from several human inspectors, and so there H does not take integer values either.

In order to infer the human classification H we need to specify the prior probability $\Pr(H)$. This is exactly what the human classifier is doing when reminding herself that lenses are rare, so that class-3 candidates should be considerably rarer than class-0 objects (which make up the majority of objects). In this spirit we might assign a prior based on what we expect the fractions of the different classes might be. A reasonable estimate for the number of BRGs acting as lenses is 1 in 1000, and we might hope for, say, 20 times more probable lenses than

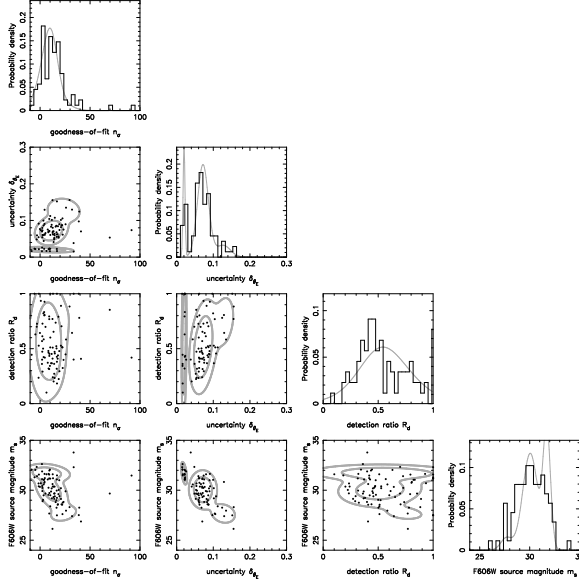


FIG. 4.— $\Pr(\mathbf{d}|H = 0)$ derived from the robot outputs (points) for the training set. Points correspond to objects classified by a human (PJM) as class $H = 0$, definitely not a lens. In this and subsequent PDF figures the contours enclose 68% and 95% of the total probability.

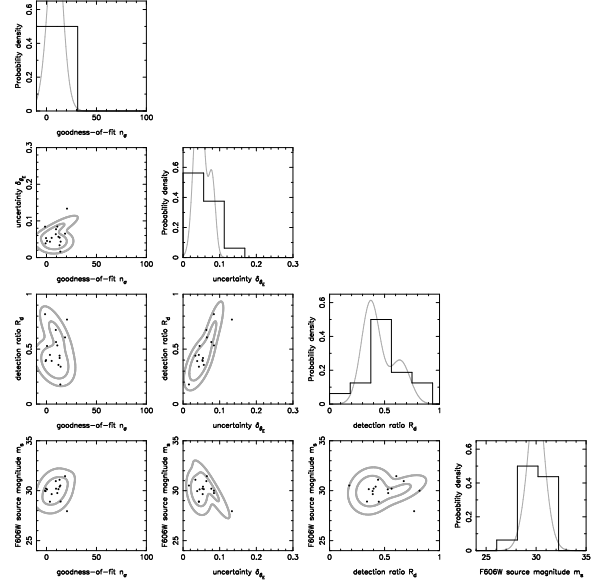


FIG. 5.— $\Pr(\mathbf{d}|H = 1)$ derived from the robot outputs (points) for the training set. Points correspond to objects classified by a human (PJM) as class $H = 1$, possibly a lens.

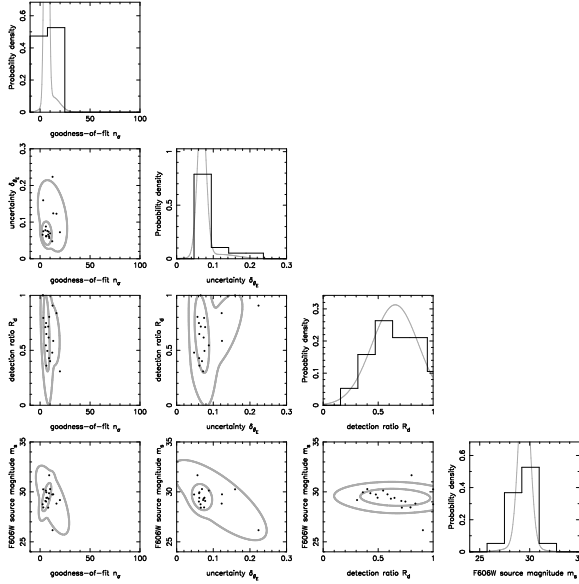


FIG. 6.— $\Pr(\mathbf{d}|H = 2)$ derived from the robot outputs (points) for the training set. Points correspond to objects classified by a human (PJM) as class $H = 2$, probably a lens.

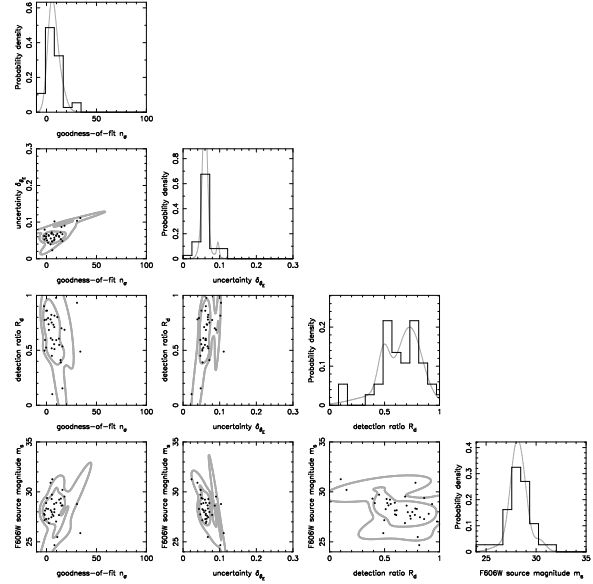


FIG. 7.— $\Pr(\mathbf{d}|H = 3)$ derived from the robot outputs (points) for the training set. Points correspond to objects classified by a human (PJM) as class $H = 3$, definitely a lens.

actual lenses. With a similar argument for class 1, we end up with $\Pr(H) = [0.9, 0.08, 0.019, 0.001]$.

With this assumption, we calculated the posterior mean H_r for each object in the training set, and compared it with its true (human-determined) value of H . This comparison is shown as a “completeness chart” in the far left-hand panel of Figure 8. Completeness $C(H; H_r)$ is defined as the percentage of objects with human class H that have robot class H_r . For example, in Figure 8, 19% of objects with human class $H = 3$ were found to also have robot-assigned class $H_r = 3$. In this chart, the percentages sum to 100 in columns. The ideal robot would give a completeness chart that would

be white (0%) everywhere except on the diagonal, where it would be black (100% complete).

The apparently low success rate of the robot at high- H must be measured against its performance at low- H : an impressive 98% of definite non-lenses are rejected. This is just the usual trade-off between completeness and purity. Defining purity $P(H_r; H)$ as the percentage of objects with robot class H_r that actually have human class H , we can plot this as a complementary purity chart – except that now, the proportions of objects in each human class H -bin need to be realistic for the numbers to make sense. Our training set does not have realistic proportions of objects of each class (nearly half are known to

be lenses); this is fine for estimating completeness, but must be corrected when estimating purity. Here we simply adjust the calculated purities to what they would have been had the proportions been those assumed in the prior $\text{Pr}(H)$ defined above. In the purity chart, the percentages sum to 100 in rows. The ideal robot would give a purity chart that would be white (0%) everywhere except on the diagonal, where it would be black (100% pure). We show the purity chart for the realistic-prior robot in the second left-hand panel Figure 8.

High purity means high efficiency: with a realistic prior for the abundance of each class of candidates, the robot class 3 sample is 100% pure. This is certainly very encouraging for future surveys, where the human inspection is time consuming and costly. However, in the short term we might prefer a relatively impure sample of candidates to be output by the robot, in return for a higher completeness. We can achieve this by altering the prior on H , analogous to having an inspector of different *character*. An “optimistic” robot might have a prior PDF $\text{Pr}(H) = [0.05, 0.10, 0.25, 0.60]$, which, while not reflecting our expectations of the abundance of lenses at all, has the practical effect of increasing the chances of a high classification value. In the rightmost two panels of Figure 8 we show the completeness and purity of the samples generated by a robot of this character – its behavior is now such that the purity of the $H_r = 3$ bin is low (1%), while the completeness at $H = 3$ is rather high (89%). The optimistic robot’s classifications for the example systems in Figure 1 are shown in the final column of Table 1.

Finally, for comparison we also show the performance of a “naive” robot – one whose prior is uniform in H – in Figure 9. While this is something of a compromise between optimism and realism, it is not designed to be such; it is neither complete enough nor pure enough to be useful. This should not be a surprise: the prior associated with this robot is one of maximal ignorance. We summarize the prior PDFs associated with each robot character in Table 3.

TABLE 3
ROBOT CHARACTERS AND CORRESPONDING PRIOR PDFs $\text{Pr}(H)$.

Character	$\text{Pr}(H = 0)$	$\text{Pr}(H = 1)$	$\text{Pr}(H = 2)$	$\text{Pr}(H = 3)$
Realistic	0.900	0.080	0.019	0.001
Optimistic	0.050	0.100	0.250	0.600
Naive	0.250	0.250	0.250	0.250

If an unrealistic prior is employed, a 100% pure sample of discovered lenses can be generated by a final human classification of a subset of robot-selected candidates. The cost of the optimistic robot is that in each square degree some 670 robot class-3 candidates must be visually inspected by a human to recover the 9 lenses present. To be 100% complete in human class $H = 3$ systems, the robot class $H_r = 2$ systems must be inspected as well – and there are some 4500 of these. As well as the percentage purities, we also show (in parentheses) on the purity charts in the figures the predicted numbers of objects in each bin for a 1-square degree survey area (assumed to contain 10^4 BRGs). Table 4 shows the overall completeness and purity for various search strategies – e.g. having humans inspect all objects with robot

class H_r above some threshold – making clear the trade-offs involved. We illustrate the numbers with two fiducial imaging surveys, representing approximately what is possible now using *HST* archive images, and in the future with a space-based optical survey telescope such as SNAP.

A crucial practical aspect of future large-scale surveys is the need to cope with the extreme numbers of BRGs involved. To quantify this we compute the rejection rate (the percentage of BRGs that are rejected by the robot and not passed to the human classifier), and the number of candidates needed to be inspected by humans. From this we estimate the time required to carry out the human classification step.

Table 4 shows the rejection rates and expected classification time Δt for our two fiducial imaging surveys, assuming an average of 10 seconds inspection time per object, and a team – for the SNAP survey – of 10 human inspectors. We see that a 20% complete SNAP sample generated by the realistic robot would contain 2000 lenses and no false positives, and require negligible classification time (~ 1 hour). A $\sim 90\%$ -complete sample consisting of 670,000 candidates could be generated by the optimistic robot, and human-classified in 5 weeks. We note that the CPU time (in 2008) for the current (and unoptimized) robot, on a 100-node compute farm, is approximately 2 hours per square degree, or 10 weeks for the SNAP survey.

To put this in context, the M07 search was carried out by one of us (LAM) inspecting “3-color” JPG images of all 63 ACS frames, a procedure that might be expected to be inefficient and prone to error. Indeed, the search took 10 minutes per frame, or 60 hours per sq degree. At the same rate the 1000-square degree survey would take 10 full-time workers 3 years to complete. Just targeting massive galaxies and inspecting sequences of small cutout images leads to a significant increase in efficiency (e.g. Fassnacht et al. 2004; Faure et al. 2008); however, visual inspection of every elliptical galaxy would still take 70 weeks with the same inspection team. While this is a factor of 2 improvement over the EGS search rate, the robot brings the cost down further by reducing the number of systems needed to be human-inspected: at $\sim 90\%$ completeness the BRG rejection rate is $\sim 90\%$. Furthermore, we found that displaying the candidates to the human classifier via a “one-click” web classification tool led to a significant reduction in the time needed to assess each one. Optimizing the information at the inspectors’ disposal should allow human classification to be performed at an average rate of just a few seconds per candidate. The survey classification time estimates in Table 4 are therefore quite conservative.

4.5. The accuracy of the robot outputs

We now investigate the robot’s modeling results for the 54 simulated lenses classified as $H = 2$ (17 objects) and $H = 3$ (37 objects). How accurate, and hence useful, are the lens model parameters inferred by the robot? Since the lens model used by the robot is simpler than that used to generate the simulations, we restrict ourselves to an investigation of the Einstein radius, which we might hope to infer reasonably accurately given the relatively small shears and ellipticities involved in the simulations. We have the true, underlying values of θ_E for each sys-

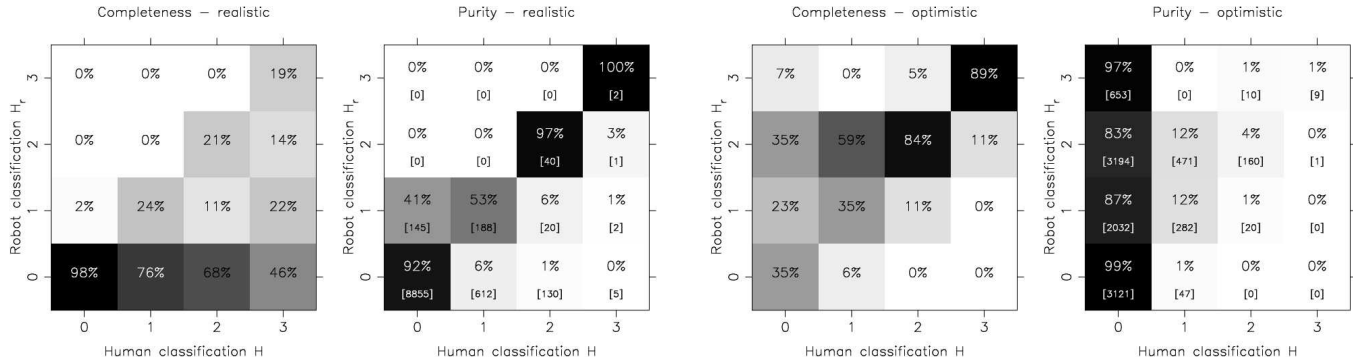


FIG. 8.— Left two panels: completeness (left) and purity (right) charts for a *realistic* prior distribution of H -values, namely one where the object classifications are as expected given what we know about the relative scarcity of gravitational lenses. Right two panels: same, but for an *optimistic* prior distribution of H -values, namely one where the majority of BRGs are expected to be acting as observable gravitational lenses. Completeness values are the percentages of the total number of candidates of true class H in each robot class H_r bin – these percentages sum to 100 in columns. Purity values are the percentages of the total number of candidates in each robot class H_r bin that have true class H – these percentages sum to 100 in rows. The numbers in parentheses on the purity charts are the approximate expected numbers of objects in each bin for a 1 square-degree survey.

TABLE 4
LENS SEARCH STRATEGIES, YIELDS AND STATISTICS.

Strategy		HST yield (1 deg ² , 10 ⁴ LRGs)			SNAP yield (1000 deg ² , 10 ⁷ LRGs)			Statistics		
Character	H_r cut	N_{cand}	Δt	N_{lens}	N_{cand}	Δt	N_{lens}	Rejection rate (%)	Purity (%)	Completeness (%)
		(man-hours)			(team-weeks)					
realistic	$H_r \geq 0.5$	399	1	5.4	399000	2.8	5400	96	1.4	54
	$H_r \geq 1.5$	43	0	3.2	43000	0.3	3200	100	7.5	32
	$H_r \geq 2.5$	2	0	1.9	2000	0	1900	100	100	19
optimistic	$H_r \geq 0.5$	6832	19	10	6832000	47.4	10000	32	0.1	100
	$H_r \geq 1.5$	4497	12	10	4497000	31.2	10000	55	0.2	100
	$H_r \geq 2.5$	672	2	8.9	672000	4.7	8900	93	1.3	89
naive	$H_r \geq 0.5$	5769	16	10	5769000	40.1	10000	42	0.2	100
	$H_r \geq 1.5$	679	2	8.4	679000	4.7	8400	93	1.2	84
	$H_r \geq 2.5$	89	0	6.5	89000	0.6	6500	99	7.3	65

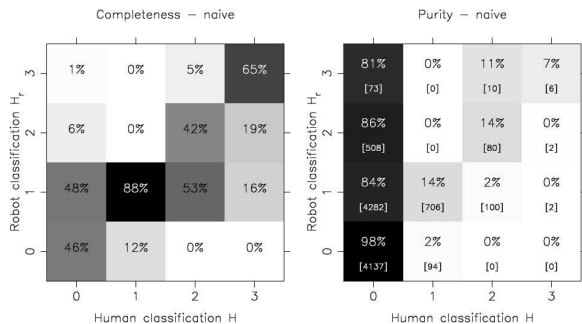


FIG. 9.— Completeness (left) and purity (right) charts for a *naive* prior distribution of H -values, namely one where all classifications are considered equally likely to occur.

tem, which we denote as $\hat{\theta}_E$.

In the left-hand panel of Figure 10 we plot histograms of $\Delta\theta_E = (\theta_E - \hat{\theta}_E)/\delta\theta_E$ for systems with human class $H = 3$ and $H = 2$ (which should each look like a Gaussian centered on zero having width unity). A peak of roughly correct width and centroid can be seen for the robust ($H = 3$) lenses, indicating that the robot’s modeling is quite meaningful in some cases but somewhat inaccurate in others. However, the histogram has significant tails, especially at large inferred θ_E . Some of this positive tail will be due to the presence of external convergence in the simulated image, but only at the few percent level. For the less convincing candidates, the histogram is broader with a less pronounced central peak,

as expected.

We might also hope to use the robot output to learn about the source galaxy: in the right-hand panel of Figure 10 we plot a similar histogram of $\Delta m_s = (m_s - \hat{m}_s)$. While we do not infer an uncertainty δm_s , the unit width Gaussian still provides a useful reference. A ~ 2 mag offset in the unlensed source magnitude can be seen, reflecting the inability of the lens model to account for all the flux. This is a consequence of using necessarily (to save CPU time) inaccurate lens models: when the model does not quite predict the image correctly, there is some mismatch between the different multiply-imaged pixels’ values. The minimum-filtering process then leads to an underestimate of the corresponding source plane pixel value. At the edges of the detected image features, this can lead to an unwanted zero value in the source plane, and so to an inferred source that is not only too faint, but also too small. The total flux of the source is then underestimated, and the rescaling performed before calculating n_σ is not enough to recover the lost flux.

The robot’s source magnitude estimates are therefore biased low. While not useful for source studies, m_s is still a valid indicator of the model quality; indeed, the discussion above shows why this so.

5. BLIND TESTING ON THE EGS SURVEY

Having calibrated the lens-finding robot on the training set, we now present its application to the 60 remaining EGS “survey” fields (Section 4.1). Table 5 summa-

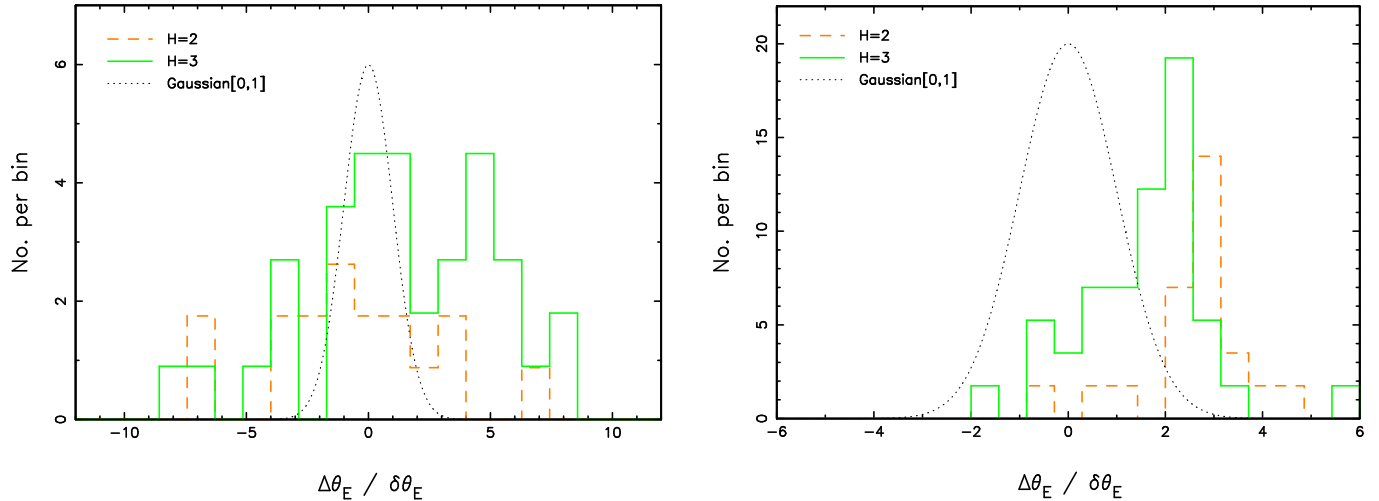


FIG. 10.— Left: accuracy of the model parameter θ_E and its “uncertainty” $\delta\theta_E$. Plotted are histograms of $\Delta\theta_E = (\theta_E - \widehat{\theta}_E)/\delta\theta_E$ for the top two human classes, compared with a Gaussian of mean zero and width 1. Right: similar plot for the inferred (unlensed) source magnitude (in the F606W band) m_s – here there is no uncertainty δm_s , but the unit width Gaussian still provides a useful scale for comparison.

TABLE 5
EGS SEARCH STRATEGIES, YIELDS AND STATISTICS.
PURITY P , COMPLETENESS C , AND REJECTION RATE R ARE ALL GIVEN AS PERCENTAGES.

Character	H_r cut	$N(H=3)$	$N(H \geq 2)$	R	$P(H=3)$	$P(H \geq 2)$	$C(H=3)$	$C(H \geq 2)$
realistic	$H_r \geq 2.5$	0	0	100	0.0	0.0	0	0
	$H_r \geq 1.5$	0	1	96	0.0	2.4	0	10
optimistic	$H_r \geq 2.5$	1	4	89	1.0	3.8	33	40
	$H_r \geq 1.5$	3	9	46	0.6	1.7	100	90

rizes the results of this run. All 988 lens candidates in these fields were visually inspected by a subset of the authors (PJM, DWH, LAM, MB, CDF), and their H -values simply averaged. (As noted before, this gives non-integer values of H .) The color images, before and after lens galaxy subtraction, were displayed to aid them in their decision-making via the cgi web form.

We ran both realistic and optimistic robots while performing the automated classification; Table 5 shows the statistics from these runs. Allowing for the small numbers involved, we find that the completeness and purity achieved by the robot are consistent with the predictions from the training set. With the realistic prior we find that none of the three $H = 3$ systems are recovered, consistent with the expected low completeness (Table 4). With the optimistic prior, we achieve 100% completeness in $H = 3$ systems when setting the robot classification threshold to $H_r \geq 1.5$, and 33% completeness with $H_r \geq 2.5$. That the latter is slightly lower than expected is a reflection on the complexity of two of the systems: as noted in M07, HST J141820.84+523611.2 (the ‘‘Dewdrop’’) has a very extended source, providing a lot of confusing structure and so fairly high values for R_d and $\delta\theta_E$. HST J141735.73+522646.3 (the ‘‘Cross’’) has almost point-like images in an asymmetric pattern, caused by the combination of both internal ellipticity and external shear in the lens (e.g. M07). This leads to a poor model fit and a high value for n_σ . The rejection ratios ensuing from the optimistic search strategies (46 and 89%) match well the predictions from the training set in Table 4 (55 and 93%).

Figure 11 shows all 10 objects with human class $H \geq 2.5$ (the ‘‘A-list’’, three objects) or $1.5 < H < 2.5$ (the ‘‘B-list’’, seven objects). The robot output data are tabulated in Table 6. The B-list systems include the three that were noted during the M06 & M07 by-eye searches – four are new lens candidates (albeit of low quality). One B-list system was rejected by the robot, a result of its large image separation.

These four new B-list candidates illustrate an important point, namely that automated searches ameliorate the problem of human error in a by-eye search. By focusing on the few galaxies consistent with being lenses, the distractions of the rest of the image are removed and there is less chance of missing an interesting object.

6. DISCUSSION

In this Section we first identify several areas where our robot’s performance could be improved, and then compare our approach with others suggested in the literature.

6.1. A more extensive training dataset

The blind test on real survey data described in Section 5 suggests that our simulations are sufficiently realistic to give us an accurate PDF for lens candidate classification, although a larger sample of known lenses would assist here. For example, the *HST*/ACS images taken during the SLACS survey would provide a training set of some 70 galaxy-galaxy strong lenses (Bolton et al. 2008). However, we must be careful to match the robot’s training set with the kinds of lenses expected to be *found in high resolution imaging data*. The selection function of the SLACS lenses is quite different, favoring low redshift lens galaxies and high magnification image configurations

(Einstein rings). While it may be argued that the latter is a desirable property of the target lenses, if we seek to find all lenses we need to educate the robot accordingly. One option for future work would be to use the entire EGS survey (as well as the simulated lenses) as a training set – although some care may be needed when applying the robot to new data of different depth and resolution. If our training set is assumed adequate, then two sources of incompleteness and inefficiency remain. One is the treatment of the training set, and the other is the lens modeling itself.

6.2. More accurate PDF modeling

It can be seen in Figures 4–7 that there are a few outliers to the derived PDFs, indicating that these model distributions are a somewhat lossy compression of the information in the training set. One way of correcting this would be to increase the complexity, and therefore inclusiveness, of the PDF models to reduce the number of outliers. However, the problem of degeneracy between the 4 different PDFs remains – this can be broken by increasing the dimensionality of the robot output data-space. While an exhaustive investigation of the individual cases is beyond the scope of this paper, we make the following general suggestion for future work. Most of the bright red objects passed to the robot for lens-modeling are *not* massive elliptical galaxies; these should give complex residual images even when the lensing-consistent flux is subtracted. Some quantitative morphology analysis of such maps might produce a useful extra dimension to use in ruling out non-lenses. Likewise, the pre-selection of BRG candidates could be improved, using some measure of concentration to favor the massive galaxies.

One disadvantage of the approach taken here is that we treat the four classifications ($H = 0, 1, 2, 3$) as exclusive and unrelated ‘‘bins’’ into which lens candidates fall; that is, we make no use of the fact that there is really a continuum from $H = 0$ to $H = 3$, and that $H = 1$ is between $H = 0$ and $H = 2$, and that $H = 0$ is very far from $H = 3$. A more sophisticated approach would make use of this continuity information, perhaps by working with the five-dimensional distribution of the four scalars *and* H ; that is, treating H as a fifth scalar to be predicted using the other four. A larger training set, or a training set classified by a larger number of humans, could also effectively increase the granularity of the H -statistic and provide a better basis for treating the classification as a continuum rather than a discontinuous set of exclusive and unrelated bins.

6.3. More accurate lens modeling

The lens modeling itself could be made cleaner at the same time as improving this pre-selection: fitting the BRG light with a bulge+disk light profile may better suppress the symmetrical disk-like residuals that can mimic lensed images, while providing some quantitative estimate of galaxy type (and hence mass). In the future, with surveys in many filters we can hope to extend this modeling to include the photometric redshift and stellar population properties of the BRG, and use the fundamental plane to estimate the BRG mass directly.

While the above desiderata may improve the efficiency of the lens search, they all favor smooth, clean lens galaxies, and sparsely populated source planes. This approach

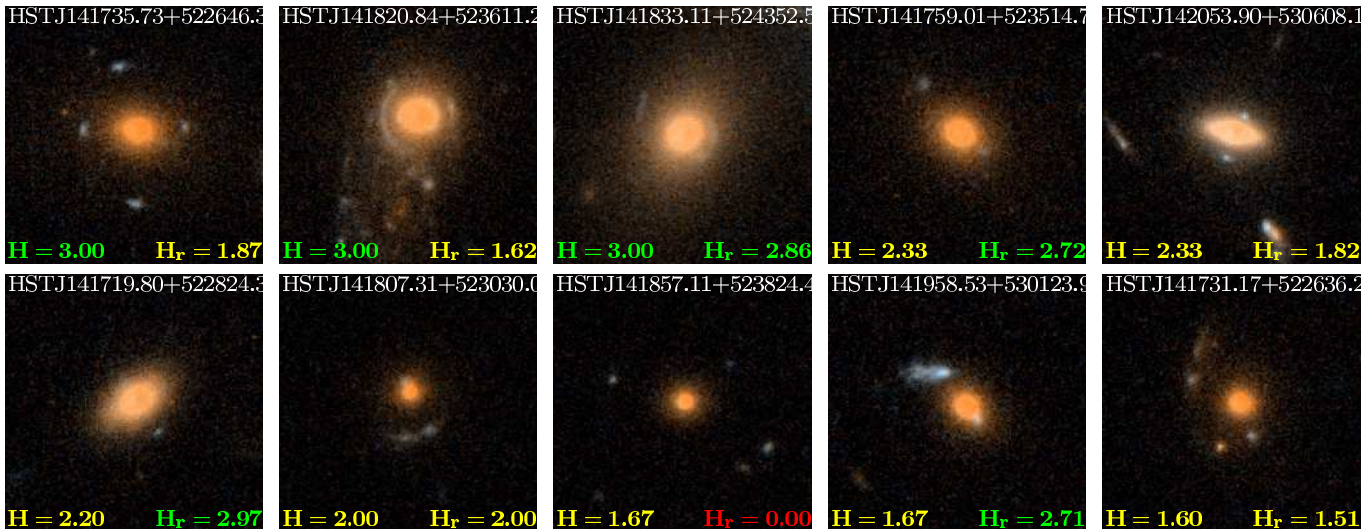


FIG. 11.— Automated lens search candidates in the EGS survey area. Candidates are sorted (left to right, top to bottom) by their human classification parameter, H – all 10 objects with $H > 1.5$ are shown. Both human and robot classification parameter (H_r) are shown overlaid on the images, with color scheme green $\rightarrow H = 3$, amber $\rightarrow H = 2$ and red $\rightarrow H = 1$. All cutout images are 6 arcsec on a side.

TABLE 6
ROBOT OUTPUTS FOR THE 10 LENS CANDIDATES IN FIGURE 11.

Object name	Position in Figure 11	n_σ	θ_E (arcsec)	$\delta\theta_E$ (arcsec)	R_d	Source magnitude AB, F606W	Robot class (H_r)	Human class (H)
HSTJ141735.73+522646.3	(1,1)	13.23	0.96	0.07	0.60	30.42	1.87	3.00
HSTJ141820.84+523611.2	(2,1)	4.08	0.66	0.14	0.69	27.92	1.62	3.00
HSTJ141833.11+524352.5	(3,1)	4.11	0.84	0.06	0.62	28.40	2.86	3.00
HSTJ141759.01+523514.7	(4,1)	5.07	0.96	0.06	0.57	28.84	2.72	2.33
HSTJ142053.90+530608.1	(5,1)	7.19	0.54	0.04	0.31	29.56	1.82	2.33
HSTJ141719.80+522824.3	(1,2)	-1.18	0.60	0.04	0.75	29.62	2.97	2.20
HSTJ141807.31+523030.0	(2,2)	1.69	0.66	0.16	1.00	29.29	2.00	2.00
HSTJ141857.11+523824.4	(3,2)	99.00	0.00	99.00	0.00	99.00	0.00	1.67
HSTJ141958.53+530123.9	(4,2)	1.21	0.66	0.07	0.48	27.96	2.71	1.67
HSTJ141731.17+522636.2	(5,2)	21.31	1.08	0.07	0.59	28.75	1.51	1.60

is somewhat justified for some of our strong lensing science goals, i.e. those that require samples of massive regular elliptical galaxies whose lensing effects are easily modeled. In fact, one of the attractive aspects of the future imaging surveys is that they will be capable of sampling further down the lensing cross-section distribution, to where the lens galaxies are higher redshift, and/or less bulge-dominated. We have shown that our approach can deal with massive galaxies that do have, for example, disk components, but at the cost of enlarging the size of the visual inspection candidate list. If we want to find more exotic disk or complex lenses, then the robot’s modeling capabilities must be increased accordingly. The pre-selection can likely be made much more stringent (e.g. selecting close pairs of BRGs) – in which case a purely visual inspection may be the most effective strategy. However, we already see in the case of the EGS lenses that more than three lens model parameters are required for a good fit to the data: more work is required on making such flexible lens fits feasible in the available CPU time.

An unwelcome side-effect of poor lens-modeling is that the output parameters may not be useful for some other desirable follow-on work. For example, the source plane photometry performed in this work is not accurate enough to estimate the photometric redshift of the source. This should probably not be a concern – even

10^4 new lenses, once found in the SNAP survey for example, could be re-modeled straightforwardly given the computing power assumed in Table 4.

Finally, it is worth revisiting the assumptions made in our lens modeling algorithm. Perhaps the most important is our neglect of the PSF. For the high resolution image surveys we have restricted ourselves to, we expect this not to be a problem for the more numerous extended galaxy-source lenses. However, we should not be surprised to find the robot failing to detect lensed quasars, especially if they are very bright. A more advanced lens modeler would have to incorporate some form of deconvolution; the most stable way to do this is to work with a model source and infer its parameters by predicting the image plane. However, this will add parameters to the model and prevent us using the efficient “minimum-filtering” scheme. Nevertheless, detecting bright lensed quasars would require the PSF to be taken into account properly, as would extending our approach to ground-based data, with its larger PSF width to source size ratio.

6.4. A more objective classification scheme

In order to bypass the more straightforwardly inferred human classification parameter, and instead answer the question “Is this a gravitational lens or not?” we would have to do the following: for each conceivably massive,

distant galaxy in a large imaging survey, search the entire space of all reasonable models for that galaxy’s lensing potential, and search the entire space of reasonable distributions of resolved and unresolved background sources in angle, redshift, and color, looking for a model to explain the morphology observed in and around the galaxy image. If, in this enormous space, there is a reasonable model for the potential and a reasonable model for the background sources that explains a significant and not fine-tuned portion of the intensity in and around the image of the lensing galaxy, then that galaxy is a very strong candidate for a multiply-imaging lens. The null model against which this would be compared would be that where all features in the elliptical-subtracted image are assumed unlensed. The key point is that the lensing hypothesis is potentially simpler for comparable (and perhaps better) goodness of fit, since fewer individual sources need to be fitted.

In practice, it is not currently possible to implement this scheme in full. As previously discussed, at present it is not practical to perform fully general lens modeling for every object. Perhaps more importantly, there is also currently no reliable way to determine which parts of the image of a putative lensing galaxy are part of that galaxy (or foreground) and which originate from background sources. For this we would need a comprehensive understanding of galaxy morphology quantified as a complex joint prior for the morphology parameters. While there are promising signs of such a formalism being developed (e.g. Lotz et al. 2004; Massey et al. 2004a), we are not there yet. This means that, at present, there is no quantitative meaning to the words “reasonable,” “significant,” and “not fine-tuned,” and so the usual evidence ratio used for model selection is not available to us.

Nonetheless, the method we have described here represents a first attempt at the model-oriented lens searching scheme, including a number of necessary approximations and simplifications. Its extension to more powerful models and fitting algorithms is straightforward, and we leave this to future work. The quantification of non-lens galaxy morphology presents a greater challenge.

6.5. Comparison with other automated lens detection algorithms

Most of the automated lens detection schemes proposed to date have focused on finding curved arc-like structures (Lenzen et al. 2005; Seidel & Bartelmann 2007; Alard 2007; Kubo & Dell’Antonio 2008). These have the benefit of finding lenses by their sources, not their lens galaxies – an important distinction for lens-statistics studies (e.g. Keeton 2002; Kochanek 2006) and for finding dark gravitational lenses. While none of these methods rely on the subtraction of the lens galaxy light before applying the algorithms, it would seem profitable to do so when searching for galaxy-scale lenses. All include a final human inspection step to provide quality control.

The Ringfinder algorithm (Gavazzi et al in preparation, Cabanac et al. 2007) does include the subtraction of the lens light: as this is modeled by rescaling the reddest available image, the method is restricted to multi-filter data. It was designed for the CFHT legacy survey ground-based data, and so represents the first attempt at specifically finding galaxy-scale lenses robotically, from

the ground. While the analysis of the blue residuals is more ad-hoc, the results could in principle be trained in the same way we have described here.

The arc-detection algorithm used by Estrada et al. (2007) in searching the SDSS images shares a key feature with our robot: they use a neural network to assess their (different) 4 data that describe each candidate arc. The probabilistic framework presented here can itself be viewed as a simple machine-learning process. Although crude (and in fact, hand-made), our framework does have the important benefit of providing some the insight into the problem. A fruitful line of future enquiry could be to replace our robot’s PDF (with its dependence on a limited data vector \mathbf{d}) with a neural network; the natural extension of this would then be to increase the number of inputs to be the pixels of the image itself. This approach would perhaps solve the problem of the non-lens galaxy morphology as well.

7. CONCLUSIONS

We have developed a novel approach to the automated detection and classification of strong galaxy-scale gravitational lenses in high resolution imaging surveys. After training our software robot on simulated and real *HST* data we draw the following conclusions:

- For high resolution data and sufficiently faint and extended images, we can neglect the PSF and reduce the complexity of the lens model to three parameters, generating the unlensed source plane by a simple and robust ray-tracing and minimum-filtering scheme. In this way, our robot is able to return crude lens models that predict the images seen in both simulated and real galaxy-scale lenses.
- While the Einstein radius and source magnitude returned by the robot are not yet accurate enough for further use, improvements in the lens modeling should make these parameters useful. The automated nature of the detection process means that the selection function is well-defined, such that measuring e.g. $dn/d\theta_E$ should be meaningful.
- Using a set of data derived from the lens model, we infer for each candidate the classification parameter H that a human inspector would have assigned it. This is a well-defined procedure that can be calibrated straightforwardly using a large sample of simulated lenses and known non-lenses; the calibration information is compressed as a set of PDFs whose estimation comprises the “training” of the robot. While some systems in the training set remain as outliers to the model distribution, this does not have a catastrophic effect on the automated classification.
- The completeness and purity of any survey are partly determined by the prior PDF on the classification parameter, in our case $\Pr(H)$. A realistic prior distribution of H -values heavily favors the classification $H = 0$ (on the grounds that they are known to be much more common), and predicts higher class objects to be correspondingly rare: it makes the search efficient, with any loss of completeness being due to the inadequacies of the modeling process. Setting a threshold of $H_r \geq 2.5$,

we find a purity of $\sim 100\%$ at a completeness of $\sim 20\%$.

- We can choose to improve the completeness at the expense of the purity and efficiency by changing the prior PDF, which is the analog of employing a classifier of different *character*. A more “optimistic” classifier would be happy to see many more high class objects, and at least at present this seems necessary to achieve 100% completeness. The price of high completeness is a low rejection rate: with the optimistic robot threshold set to $H_r \geq 2.5$, we find a rejection rate of $\sim 90\%$ at a completeness of $\sim 90\%$.
- A realistic robot may be most appropriate for future large imaging surveys where human inspection is costly. A 1000 square degree survey with a space telescope such as SNAP would contain $\sim 10^7$ BRGs and $\sim 10^4$ lenses; the current realistic robot’s sample would comprise 2000 of these, with no inspection required.
- An optimistic robot is more appropriate for present-day lens searches, where the numbers are small enough for human inspection to be cheap, and where every new lens counts. A search area of 1 square degree, such as that provided by the *HST*/ACS archive, would lead to an optimistic robot sample of ~ 5000 candidates, with the human classification taking ~ 1 day.
- Applying the optimistic robot to the EGS survey, we recovered all three human class-3 lenses, and all but one of the three human class-2 lens candidates from M06 and M07. We also discovered four new human class-2 lens candidates.

At the time of writing, the era of wide-field imaging from space is still ~ 1 decade away. Continuing to train

our software robot on *HST* data, we should be optimistic about the prospects of a feasible search generating a well-defined statistical sample of galaxy-scale strong lenses from an imaging survey like that of SNAP. The approach we have described here is maximally informative, in that it incorporates our expectations about the typical lenses in the universe. However, perhaps the biggest challenge will be discovering the more complex and unexpected strong lenses yet to be seen.

We thank Raphael Gavazzi, Tommaso Treu, Eric Morganson, Elisabeth Newton, Marco Lombardi, Ole Moller and Konrad Kuijken for useful discussions, Jean-Paul Kneib for much encouragement, and Cecile Faure for a careful reading of the manuscript. We are grateful to the EGS team for providing their high level science products at an early stage in the project. DWH thanks the staff of the Spitzer Science Center for their hospitality during his visit when some of this work was carried out. Support for this work was provided by NASA through grant number HST-AR-11289 (the HAGGLEs project) from the Space Telescope Science Institute, which is operated by AURA, Inc., under NASA contract NAS 5-26555. The work of PJM, RDB and MB was supported in part by the U.S. Department of Energy, under contract number DE-AC02-76SF00515 at the Stanford Linear Accelerator Center. The work of RDB was supported in part by a National Science Foundation grant, “Gravitational optics, dark matter, and the evolution of faint galaxies,” and by a U.S. Department of Energy Computational Astrophysics Consortium grant, “3. supernovae, gamma-ray bursts, and nucleosynthesis”. The work of PJM was supported by the TABASGO foundation in the form of a research fellowship. The work of LAM was carried out at the Jet Propulsion Laboratory, California Institute of Technology, under a contract with NASA.

REFERENCES

- Alard, C. 2007, MNRAS, 382, L58
Aldering, S. C. G., et al. 2004
Allam, S. S., Tucker, D. L., Lin, H., Diehl, H. T., Annis, J., Buckley-Geer, E. J., & Frieman, J. A. 2007, ApJ, 662, L51
Bertin, E., & Arnouts, S. 1996, A&AS, 117, 393
Bolton, A. S., Burles, S., Koopmans, L. V. E., Treu, T., Gavazzi, R., Moustakas, L. A., Wayth, R., & Schlegel, D. J. 2008, ApJ, submitted
Bolton, A. S., Burles, S., Koopmans, L. V. E., Treu, T., & Moustakas, L. A. 2006, ApJ, 638, 703
Bolton, A. S., Burles, S., Schlegel, D. J., Eisenstein, D. J., & Brinkmann, J. 2004, AJ, 127, 1860
Bradač, M., Schneider, P., Lombardi, M., Steinmetz, M., Koopmans, L. V. E., & Navarro, J. F. 2004, A&A, 423, 797
Browne, I. W. A., et al. 2003, MNRAS, 341, 13
Bunker, A. J., Moustakas, L. A., & Davis, M. 2000, ApJ, 531, 95
Cabanac, R. A., et al. 2007, A&A, 461, 813
Capelo, P. R., & Natarajan, P. 2007, New Journal of Physics, 9, 445
Davis, M., et al. 2007, ApJ, 660, L1
de Vaucouleurs, G. 1948, Annales d’Astrophysique, 11, 247
Estrada, J., et al. 2007, ApJ, 660, 1176
Fassnacht, C. D., Moustakas, L. A., Casertano, S., Ferguson, H. C., Lucas, R. A., & Park, Y. 2004, ApJ, 600, L155
Faure, C., et al. 2008, ApJS, 176, 19
Hogg, D. W., Blandford, R., Kundic, T., Fassnacht, C. D., & Malhotra, S. 1996, ApJ, 467, L73
Holder, G. P., & Schechter, P. L. 2003, ApJ, 589, 688
Inada, N., et al. 2003, Nature, 426, 810
Keeton, C. R. 2002, ApJ, 575, L1
Kochanek, C. S. 1991, ApJ, 373, 354
Kochanek, C. S. 2006, in Gravitational Lensing: Strong, Weak & Micro, ed. G. Meylan, P. Jetzer, & P. North, Lecture Notes of the 33rd Saas-Fee Advanced Course (Springer-Verlag: Berlin)
Kochanek, C. S., & Dalal, N. 2004, ApJ, 610, 69
Kochanek, C. S., Mochejska, B., Morgan, N. D., & Stanek, K. Z. 2006, ApJ, 637, L73
Koopmans, L. V. E. 2005, MNRAS, 363, 1136
Koopmans, L. V. E., Treu, T., Bolton, A. S., Burles, S., & Moustakas, L. A. 2006, ApJ, 649, 599
Kormann, R., Schneider, P., & Bartelmann, M. 1994, A&A, 284, 285
Kubo, J. M., & Dell’Antonio, I. P. 2008, MNRAS, 385, 918
Leauthaud, A., et al. 2007, ApJS, 172, 219
Lenzen, F., Scherzer, O., & Schindler, S. 2005, A&A, 443, 1087
Lotz, J. M., Primack, J., & Madau, P. 2004, AJ, 128, 163
Marshall, P., Blandford, R., & Sako, M. 2005a, New Astronomy Review, 49, 387
Marshall, P. J., Moustakas, L. A., Hogg, D. W., Bradac, M., Fassnacht, C. D., & Blandford, R. D. 2005b, in American Astronomical Society Meeting Abstracts, Vol. 207, American Astronomical Society Meeting Abstracts, 200.03
Marshall, P. J., et al. 2007, ApJ, 671, 1196
Massey, R., Refregier, A., Conselice, C. J., David, J., & Bacon, J. 2004a, MNRAS, 348, 214
Massey, R., et al. 2004b, AJ, 127, 3089

- Mitchell, J. L., Keeton, C. R., Frieman, J. A., & Sheth, R. K. 2005, *ApJ*, 622, 81
- Moustakas, L. A., Marshall, P., & AEGIS Collaboration. 2006, in *Bulletin of the American Astronomical Society*, Vol. 38, Bulletin of the American Astronomical Society, 926
- Moustakas, L. A., et al. 2007, *ApJ*, 660, L31
- Myers, S. T., et al. 2003, *MNRAS*, 341, 1
- Oguri, M. 2007, *ApJ*, 660, 1
- Oguri, M., Inada, N., Pindor, B., Strauss, M. A., Richards, G. T., Hennawi, J. F., Turner, E. L., Lupton, R. H., Schneider, D. P., Fukugita, M., & Brinkmann, J. 2006, *AJ*, 132, 999
- Oguri, M., et al. 2004, *ApJ*, 605, 78
- Pindor, B. 2005, *ApJ*, 626, 649
- Pindor, B., et al. 2006, *AJ*, 131, 41
- Poindexter, S., Morgan, N., & Kochanek, C. S. 2008, *ApJ*, 673, 34
- Ratnatunga, K. U., Griffiths, R. E., & Ostrander, E. J. 1999, *AJ*, 117, 2010
- Seidel, G., & Bartelmann, M. 2007, *A&A*, 472, 341
- Smail, I., et al. 2007, *ApJ*, 654, L33
- Suyu, S. H., Marshall, P. J., Blandford, R. D., Fassnacht, C. D., Koopmans, L. V. E., McKean, J. P., & Treu, T. 2008, *ApJ*, submitted (arXiv:0804.2827)
- Treu, T., & Koopmans, L. V. E. 2004, *ApJ*, 611, 739
- Treu, T., et al. 2005, *ApJ*, 633, 174
- Turner, E. L., Ostriker, J. P., & Gott, III, J. R. 1984, *ApJ*, 284, 1
- Walsh, D., Carswell, R. F., & Weymann, R. J. 1979, *Nature*, 279, 381
- Warren, S. J., Hewett, P. C., Lewis, G. F., Moller, P., Iovino, A., & Shaver, P. A. 1996, *MNRAS*, 278, 139
- Willis, J. P., Hewett, P. C., Warren, S. J., Dye, S., & Maddox, N. 2006, *MNRAS*, 552
- Zepf, S. E., Moustakas, L. A., & Davis, M. 1997, *ApJ*, 474, L1